

NORTHWESTERN UNIVERSITY

Whisker Frames: A Mechanism for the Biomimetic Actuation of Rodent Whiskers

A DISSERTATION

SUBMITTED TO THE GRADUATE SCHOOL

IN PARTIAL FULFILLMENT OF THE REQUIREMENTS

for the degree

MASTER OF SCIENCE

Field of Mechanical Engineering

By

Mark Galperin

Evanston, Illinois

June 2021

Abstract

Rats and mice move their whiskers in a rapid, rhythmic motion known as whisking to sense objects in their environment. Whisking is a remarkably varied and nuanced set of motions that allows rats and mice to position their whisker arrays in a myriad of orientations, changing dynamically over the period of sensation. To achieve this, whisking rodents employ a complicated network of intrinsic and extrinsic musculature that acts on whisker follicles along the rows of the rodent whisker pad. Despite the row-wise nature of the muscular mechanics, we observed that many robotic analogues of the rodent vibrissal system actuate their whiskers via rotating columns of vectors. Column-wise configurations require a large number of motors and have no biological analogue. In this work, we took inspiration from row-wise actuation of whisker follicles to design a novel, low degree-of-freedom mechanism called Whisker Frames which orients the entire array via the relative motion of rigid bodies. We define the system hardware and fully characterize the geometry of the mechanism through a variety of vector models. Through simulated comparison to a real-life measured whisking cycle, we show that this mechanism can accurately approximate the orientations of rodent whiskers as they whisk. Furthermore, we present this low-dimensional system as a hypothetical model for reducing the dimensionality of neural control in rat sensation.

Acknowledgment

A massive thank you to Professor Hartmann and committee members Kevin Lynch and John Rudnicki for their guidance and feedback, and for the opportunity to turn this project into meaningful work.

Also, a huge thank you to Kevin Kleczka for his collaborations on the manuscript, tracking data, hardware, and frequent insights on how to improve my analysis. The project could not have gotten this far without him.

Thank you to Yifu Luo for biological insights, data, and critiques, Hannah Emnett for hardware planning, Madeline Corrigan for frequent advice and moral support, and the entire SeNSE Lab for all their generous help.

Table of Contents

Abstract.....	2
Acknowledgment.....	3
Table of Contents.....	4
List of Tables, Illustrations, Figures, Graphs	Error! Bookmark not defined.
1. Introduction	6
2. Methods	9
2.1 A 3-DOF mechanism is defined to orient a row of whiskers	9
2.2 A vector model is used to model the mechanism configuration and output orientations ...	11
2.3 A modified vector model takes two whiskers as input and reduces the input dimensionality of the system	14
2.4 Methods to compare with biological whisking	16
2.5 Biological reference angles are used to find optimally matched configurations for the mechanism	18
3. Results.....	20
3.1 Analyzing Protractions in the entire x-y plane reveals that every whisker line is tangent to a parabola	20
3.2 Degenerate configurations of the parabola cause all whiskers to converge to a point or be parallel.....	23

3.3 Non-degenerate cases of the whisker-tangent parabola permit visualization all possible whisker outputs	24
3.4 The modified vector model positions the control frame in an elliptical pattern	26
3.5 Optimal trajectories for the control frame are found using both 3-DOF and 1-DOF models	28
4. Discussion	32
4.1 Hardware model and extended applications	32
4.2 Geometric insights.....	33
4.3 Trajectory optimization.....	33
4.4 Biological analogy and dimensionality reduction.....	34
5. Supplemental Information and Derivations.....	36
S.1: Derivation of $u(y)$ and w vectors	36
S.2: Derivation of the vector r for the modified vector model.....	38
S.3: Homogenous Transformation of conic curves to the unit parabola $y=x^2$	40
S.4: Derivations of transformation parameters for $\{xy\} \rightarrow \{x'y'\}$	42
References	46

1. Introduction

Over a century of research has established the rodent vibrissal system as one of the premier models for the study of sensorimotor integration, active tactile sensing, and thalamocortical processing^[1, 2]. Rats and mice are nocturnal animals with low acuity vision^[3-8], and thus rely on their vibrissae as a primary sensory modality for obtaining information about their environment. They have about 30 vibrissae regularly arranged in rows and columns on each mystacial pad^[9, 10]. During vibrissal sensing, both species often exhibit a behavior known as “whisking” while sensing with their vibrissal arrays, in which the whiskers are rhythmically swept back and forth^[1, 2, 11, 12].

Substantial work has focused on the sensory signals acquired by whiskers and how that information is processed throughout the trigeminal pathway to barrel cortex^[13-15], ^[3, 16-21]. Our understanding of processing in these neural pathways has increased in concert with our understanding of the peripheral mechanotactile (sensory) signals that drive them^[19-27]. Although less work has aimed to characterize the whisker motor periphery, it is equally important because peripheral morphology and neural processing are closely intertwined.

Recent behavioral and neurophysiological results indicate that although whisking is fundamentally a rhythmic behavior^[28], it incorporates a remarkably varied, nuanced movement repertoire ^[29-38] that is heavily influenced by the whiskers’ interactions with the environment^[29, 31-33, 39]. Rats and mice can vary the velocity and amplitude of their whisking; the whisking of the left and right whisker arrays can be unsynchronized, with each array moving with a different phase or frequency^[12, 32, 33, 39-41]; the span of the array can vary for the same phase of the whisk^[29]; and whiskers in each array have a degree of independence^[12, 34-36]. This variability in whisking kinematics effectively allows the rat to change the position, shape, and size of the vibrissal array about its head, and the way that the rat’s search space varies across different

behavioral conditions is thought to reflect both reflexive components^[37, 39] as well as the process of directed attention^[33].

In rats and mice, whiskers are actuated by two sets of intrinsic muscles that connect adjacent follicles, as well as at least nine extrinsic muscle groups that connect to the skull ^[42]. The intrinsic “sling” muscles that connect the upper half of the caudal follicle to the lower half of the rostral follicle in the same row are thought to be primarily responsible for whisker protraction^[42]. Because these muscles only connect muscles in the same row, the minimal “unit” of actuation is a row-wise pair^[43], and thus models of the muscular systems responsible for actuating the whiskers should be primarily row-based. There have been multiple proposed row-wise models that aim to capture whisker protraction^[44, 45], but a lack of models that aim to capture the complex protraction patterns observed in the animal that minimize the number of degrees of freedom and could be used in hardware systems involving artificial whisker sensors. Most actuation systems for artificial whiskers are column-based^[46], activating individual columns of whiskers by independent motors, or cannot vary the span of the array or individual whisker spacing^[45]. Simplified models that can replicate biological whisking behaviors may provide insight into underlying control circuits or muscle synergies in the animal, as well as provide efficient means for actuating tactile sensors during active robotic exploration.

Artificial whisker-like tactile sensors for robotic applications is an active area of research. They are useful both as a means of sensing the environment, as well as tools to explore biology and the nervous system that cannot be achieved in simulation or in the real animal. Whisker sensors can localize 3D contact points, either with an active whisking approach that uses the rate of change of bending moment at the base of the whisker ^{[47],[48]}, or with a quasi-static approach^[49]; it has been shown that artificial whiskers can discriminate texture^[50]; and there have been studies that show artificial whiskers can sense fluid flow in air and water, and can be

used to detect vortices and wakes in water^[51]. We believe that there is value in being able to replicate the complex interactions between whiskers and the environment in hardware, where we have the capability to record the full “input” into the vibrissal system.

The present work describes a mechanism to actuate a row of the whisker array with three degrees of freedom, with an additional formulation that reduces the controllable degrees of freedom to one. The system is capable of changing the protraction, span, and individual whisker spacing of the row, and is designed using easily modeled “hard” components. These rows can be stacked vertically to actuate a full array using the same three degrees of freedom. This study describes the design of the system and construction of hardware implementation, presents the analytical solution for the system, characterizes the output space of actuations producible by the device, and quantifies the ability of the device to replicate biological whisker angles in an actively whisking mouse.

2. Methods

2.1 A 3-DOF mechanism is defined to orient a row of whiskers

The proposed mechanism orients an array of mechanical whisker sensors by the relative position of two rigid body “frames”, the face frame and the control frame. To introduce this mechanism, consider how individual whiskers are positioned, as shown in the schematic in Figure (2.1-A). An artificial whisker sensor (green) is fixed to a rotating joint and points a whisker to the right at an angle θ from the normal line. A stiff rod is fixed to the other side of the sensor, collinear with the whisker. The rod runs through a compound rotating/sliding joint (red), which can slide along the length of the rod and passively rotate to match the whisker orientation. The angle θ is thus controlled by the (x,y) position of the rotating/sliding joint, which from here will be referred to as the “control joint”.

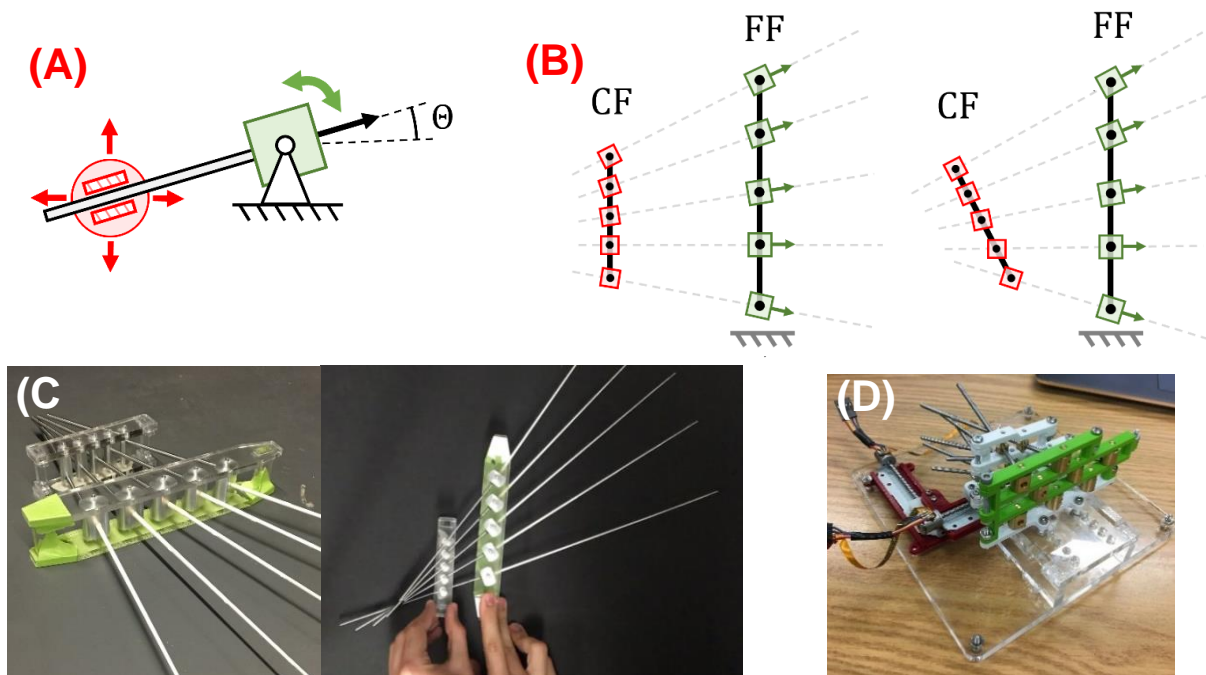


Figure 2.1 Hardware model of the Whisker Frames (A) A pair of joints that control a single whisker. A rotating/sliding “control joint” (red) and a rotating, translationally fixed rotating joint (green). (B) Multiple joint pairs are mapped onto corresponding locations on two straight line frames, the “control frame” (“CF”) and the “face frame” (“FF”). (C) Proof-of-concept hardware model consisting of

aluminium joint pieces, laser-cut frames, and steel control rods. (D) Advanced iteration of the hardware model, scaled to 5x-rat and motorized in x and y.

The mechanism in this work orients an entire *row* of whiskers by attaching the joint pair described above to two straight-line “frames” (Figure 2.1-B). Rotating joints are placed along a straight-line face frame (“FF”) and control joints are placed along a shorter straight-line control frame (“CF”). It is not important for the points to be placed at equal intervals, as they are in the figure, but it is important for the point locations on the frames to be geometrically similar, so one frame is an evenly scaled version of the other.

The control frame can move with three degrees of freedom relative to the face frame. Assuming the frames lie in the x-y plane, the control frame can rotate about its z axis and translate in the x and y direction. As the control frame moves, the rods are directed to pass through the control joints, causing the whiskers to rotate.

The preceding describes the actuation of a single row, but multiple parallel frames can be stacked on top of each other to create an array of whiskers, still being actuated with the same three degrees of freedom. In order to assess the feasibility of this device, two prototypes were constructed in hardware. The first (Fig. 2.1-C) consists of a single row and is actuated by hand, while the second (Fig. 2.1-D) contains three rows stacked vertically and is actuated by small linear stages. An additional motor would need to be added to rotate the control frame.

2.2 A vector model is used to model the mechanism configuration and output orientations

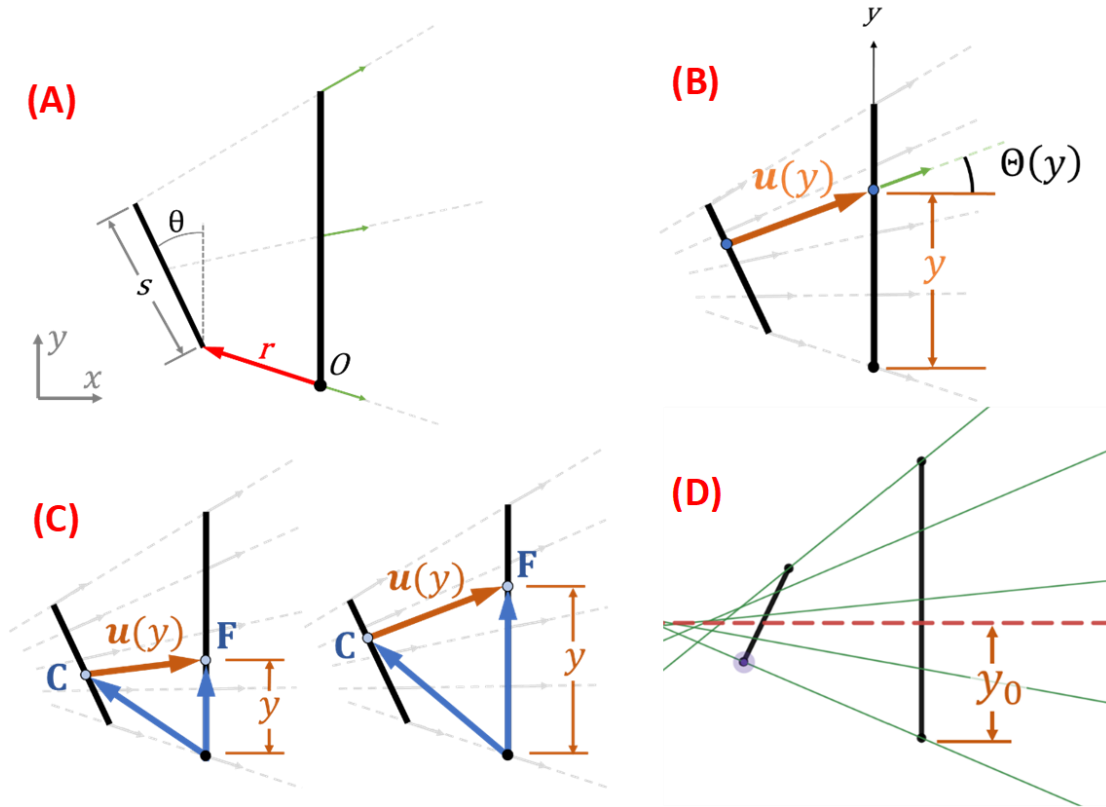


Figure 2.2 Whisker Frames Geometry (A) Vector schematic of the whisker frames mechanism. The face frame lies at the origin O of the x - y plane, and extends a unit length along the y axis. (B) The output of the system, $\Theta(y)$, is the angle a whisker would make with respect to normal to the face frame at any point y along the face frame. (C) Two examples of corresponding points (shown in blue) between the two frames. The vector $u(y)$ is the difference between the corresponding points and determines the direction of the whisker at any point y on the face frame. (D) The zero-whisker line is shown in red, at $y = y_0$.

The geometry of the mechanism was analyzed as a planar vector model, with both frames in the x - y plane. In this model, defined in Figure 2.2-A, the face frame is a unit-length line segment on the y -axis, running from the origin $(0,0)$ to the point $(0,1)$. The control frame is a line segment of length s , rotated an angle θ from the y -axis and positioned away from the origin by the vector r . Because s cannot be changed in the hardware model, it is considered a constant. The position

and length of the face frame is also fixed, attributing all degrees of freedom to the control frame. The configuration of the system is thus defined by 3 variables, forming the following configuration vector \mathbf{x} .

$$\mathbf{x} = [r_1, r_2, \theta] \in \mathbb{R}^3$$

The model's output is a continuous range of whisker orientations, defined by the angle the whisker makes with respect to the x-axis (normal to the face frame) (Figure 2.2-B). This angle is called “protraction,” and is denoted by capital theta, $\Theta(y)$. A second important parameter is the derivative of Θ with respect to the length of the face frame (or y , in this model). In this paper, this measure is called “localized spread,” (this makes reference to “spread,” a measure of the total angle covered by a whisker array as studied in Grant 2009^[29])

The vector $\mathbf{u}(y)$ must be defined to derive $\Theta(y)$. $\mathbf{u}(y)$ is defined as the vector difference between corresponding joint locations \mathbf{F} and \mathbf{C} on the face frame and is defined as follows: (see S.1 for derivation).

$$\mathbf{u}(y) = \mathbf{F}(y) - \mathbf{C}(y) = \mathbf{w}y - \mathbf{r} \quad \text{where } \mathbf{w} = [s \sin \theta, 1 - s \cos \theta]^T$$

Knowing $\mathbf{u}(y)$, a function for whisker *protraction* angles $\Theta(y)$ can be found as using ratio of the vector's components:

$$\Theta(y) = \tan^{-1} \frac{u_2}{u_1}$$

$$\Theta(y) = \tan^{-1} \frac{w_2 y - r_2}{w_1 y - r_1}$$

Localized spread is then found by differentiating with respect to y :

$$\frac{d\Theta}{dy}(y) \equiv \frac{r_1 w_2 - r_2 w_1}{[r_1 + w_1 y]^2 + [r_2 + w_2 y]^2}$$

The preceding two equations represent analytic solutions for protraction and spread of the whisker array.

Another useful result from this formulation is the location of the zero-protraction whisker, which separates the whiskers into forward and backward-facing regions. This whisker exists at the value of y such that $u_2(y) = 0$, ensuring the whisker is parallel to the x-axis.

$$w_2 y_0 - r_2 = 0$$

$$y_0 = \frac{r_2}{w_2}$$

The zero-whisker line at $y = y_0$ is illustrated as a dashed red line in figure 2.2-D. Assuming the face frame is of unit length, the value of y_0 is equal to the proportion of whiskers oriented negatively (backwards). If $y_0 < 0$, all whiskers are oriented positively (forwards), and if $y_0 > 1$, all whiskers are oriented negatively.

2.3 A modified vector model takes two whiskers as input and reduces the input dimensionality of the system

In the previous model, all three degrees of freedom are assigned to the configuration of the control frame, forming the vector of control inputs $x = [r_1, r_2, \theta]$. An alternate configuration is defined to attribute two of those degrees of freedom to the resultant whisker protractions.

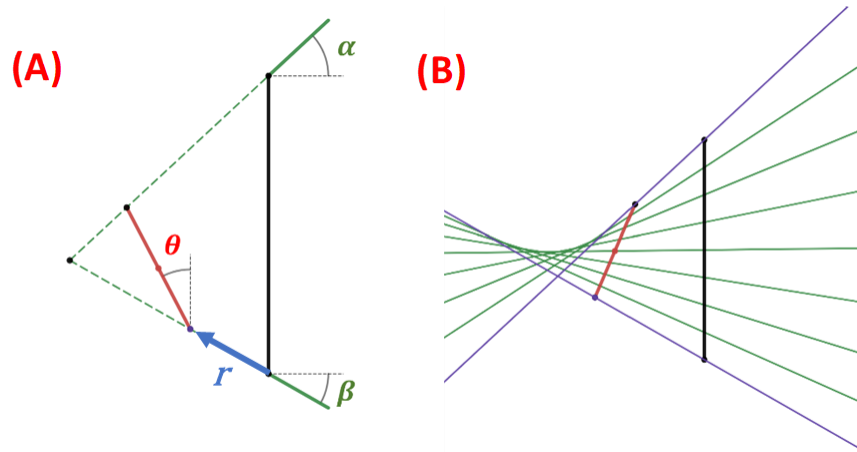


Figure 2.3 Modified vector model (A) Vector schematic of the modified model, with top and bottom whiskers oriented at angles α and β , and the control frame oriented at angle θ . r is also illustrated, but is a function of the other parameters. (B) A Desmos model of the modified model, with 9 whiskers total.

As before, the face frame is defined as the segment between (0,0) and (0,1), the length of the control frame is the constant s , and the angle of the control frame with respect to the face frame is θ . Define two angles, α and β , which are the given protraction angles for the front and back whiskers respectively. This forms the following “modified” configuration vector...

$$x_m = [\alpha, \beta, \theta]$$

As shown in Figure 2.3, the control frame is constrained to a unique position, and whiskers can be plotted between the frames. Keeping the top and bottom whiskers fixed, the system reduces to one degree of freedom for changing the shape of the resulting whiskers. To calculate the protraction of the whiskers, the vector r (now a function of θ) must be calculated, and then used

in the expression for $\mathbf{u}(y)$. The vector \mathbf{r} is found as the following matrix-vector product. For a derivation, see supplemental section S.2.

$$\mathbf{r} = \begin{bmatrix} \frac{\tan \alpha}{\tan \alpha - \tan \beta} & \frac{1}{\tan \beta - \tan \alpha} \\ \frac{1}{\cot \beta - \cot \alpha} & \frac{\tan \beta}{\tan \beta - \tan \alpha} \end{bmatrix} \mathbf{w} = M\mathbf{w}$$

Note that terms $\tan \alpha$ and $\tan \beta$ correspond to the *slopes* of the lines drawn by angles α and β .

$\mathbf{u}(y)$ can now be found by the following relation

$$\mathbf{u}(y) = \mathbf{w}y - \mathbf{r} = \mathbf{w}y - M\mathbf{w} = (yI)\mathbf{w} - M\mathbf{w}$$

$$\mathbf{u}(y) = (yI - M)\mathbf{w}$$

Like before, protraction is now defined using the arctangent of the ratio of the components of $\mathbf{u}(y)$:

$$\theta(y) = \tan^{-1} \frac{u_2}{u_1} \quad \text{and} \quad \frac{d\theta}{dy}(y) \equiv \frac{r_1 w_2 - r_2 w_1}{[r_1 + w_1 y]^2 + [r_2 + w_2 y]^2}$$

2.4 Methods to compare with biological whisking

The performance benchmark for the whisker frames mechanism is how accurately it can *mimic* the real motions of rat whiskers. To perform this comparison, a simulation of the model aims to replicate real whisker motions taken from tracked video data. In the following section, the method for processing this data to make it fit for comparison is discussed.

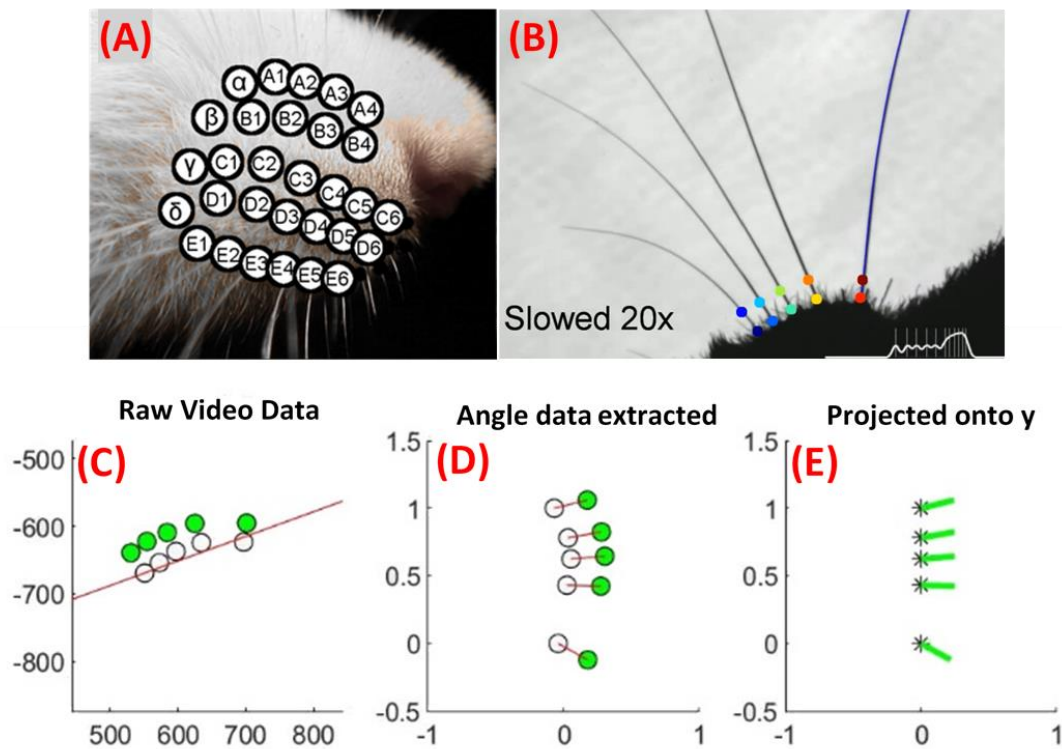


Figure 2.4 Biological reference and data preprocessing (A) 30 whiskers of the rat/mouse vibrissal array, labeled by row and number. (B) Screenshot from the 855-frame video used as the reference data for this work. (C) Raw video data (pixels) plotted in x, -y pixels to account for top-down y coordinates of video data. An angle (D) Whisker base points (white) taken from an average of eight static scans of anesthetized mice and normalized to face-frame coordinates, with tip points (green) calculated using the protraction angles in (C). (E) Projected basepoints with angles.

The rat and mouse vibrissal arrays are comprised of 30 whiskers arranged in a pattern shown in Figure 2.4-A. This pattern places whiskers in five rows, A - E, with an additional column of off-row whiskers notated by Greek letters $\alpha - \delta$. The video data studied in this work is top-down

video tracking a single non-Greek row (row C), omitting whisker C2 due to a clipped whisker. A screenshot of the video with tracking markers is shown in Figure 2.4-B.

The processing of this data takes three steps, as shown from left to right in Figure 2.4-C. In the first step, base (white) and tip (points) are plotted in pixel coordinates. An approximate angle-compensation line (red) is drawn through the points at an angle of 20 degrees from the x-axis. All whisker angles will be measured with respect to this line, which stays constant throughout the whisking cycle. Whisker protraction angles are calculated by the relative positions of base and tip points. In the second step (2.4-D), these angles are assigned to corresponding *static* points from row C of a 3D scan of mouse whisker locations, whose first and last basepoints have been normalized to lie on the face-frame points (0,0) and (0,1), with the rostral-most whisker at (0,1). In the third step (2.4-E), the basepoints are simply projected to the y-axis. Basepoints now all lie on the line segment that defines the face frame.

The data is processed by these three steps for each frame of video, producing a time series of points on the y-axis that correspond to biologically observed angles of protraction.

2.5 Biological reference angles are used to find optimally matched configurations for the mechanism

In the previous section, reference angles were mapped onto a virtual “face frame” for each time frame of an 855-frame video. With these data, an optimal configuration of the mechanism can be found at each frame, forming an error-minimizing time-trajectory for the system.

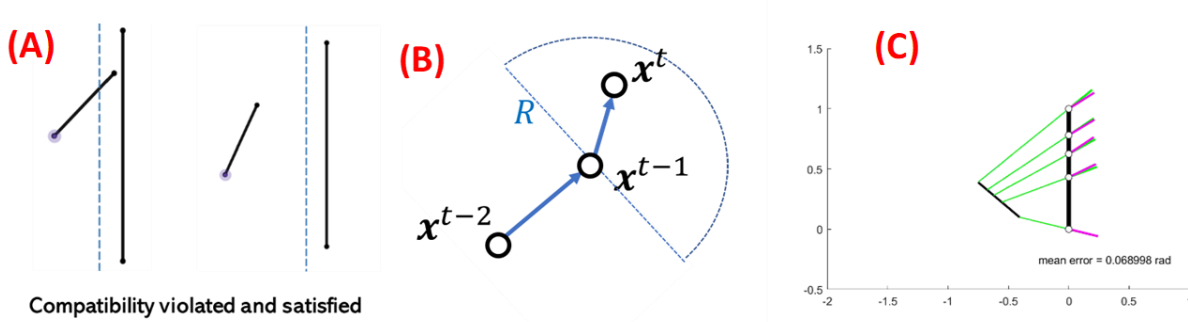


Figure 5 Trajectory Optimization (A) Compatability constraints violated (left) and satisfied (right) (B) Illustration of the combined effects of constraint g_3 and g_5 (C) A screenshot from an optimal trajectory animation.

For N video-processed whiskers, there are N whisker basepoints that lie at points y_i on the interval $(0,1)$ on the y -axis. For each basepoint, there is an associated protraction angle $\Theta_b(y_i)$ at which a whisker is oriented from that point. At a given time t , the whisker frames configuration $\mathbf{x}^t = [r_1, r_2, \theta]^T$ produces a range of whisker protractions $\Theta_w(y_i, \mathbf{x}^t)$ on the same y -interval by the protraction equations derived in section 2.2.

To find the optimal time-trajectory for the system configuration, an optimization is performed with \mathbf{x}^t as the decision variable. at each time t , the configuration \mathbf{x}^t is optimized such that the following error function is minimized, subject to the constraints g_1 - g_5

$$E(\mathbf{x}^t) = \frac{1}{N} \sum_{i=1}^N \text{abs}(\Theta_b(y_i) - \Theta_w(y_i, \mathbf{x}^t))$$

$$g_1(\mathbf{x}^t): x_1 \leq 0$$

$$g_2(\mathbf{x}^t): x_1 - s \sin(x_3) + c \leq 0$$

$$g_3(\mathbf{x}^t): (x_1^t - x_1^{t-1})^2 + (x_2^t - x_2^{t-1})^2 - R^2 \leq 0$$

$$g_4(\mathbf{x}^t): \text{abs}(x_3^t - x_3^{t-1}) - d\theta \leq 0$$

$$g_5(\mathbf{x}^t): -(x_1^t - x_1^{t-1})(x_1^{t-1} - x_1^{t-2}) - (x_2^t - x_2^{t-1})(x_2^{t-1} - x_2^{t-2}) \leq 0$$

Inequality constraints g_1 and g_2 ensure geometric compatibility: keeping the entirety of the control frame to the left of a line parallel to the face frame, a distance c away. Examples of geometric compatibility violated and satisfied are shown in Figure 2.5-A.

The other three constraints ensure *smoothness* of the resulting trajectory. Constraint g_3 keeps successive position points $[x_1, x_2]$ a maximum distance of R away from the previous point. Constraint g_4 keeps changes to x_3 , the *angle* of the control frame, below a certain small-valued $d\theta$. Constraint g_5 uses two previous variable values to smooth the direction of change, keeping all successive points beyond the line perpendicular to the previous change in position. A schematic of the combined effects of g_3 and g_5 is shown in Figure 2.5-B.

Minimal-error trajectories were generated using a nonlinear optimizer (from the MATLAB optimization toolbox) for 3-DOF trials and using a homemade “brute-force” optimizer for the 1-DOF trials.

3. Results

3.1 Analyzing Protractions in the entire x-y plane reveals that every whisker line is tangent to a parabola

To better understand the geometry of the system, whisker orientations on all parts of the x-y plane should be analyzed. Although $u(y)$ does describe all whisker orientations along the face frame, it does not determine the orientation of a whisker that passes through an arbitrary point off the face frame, as its domain is limited to the y-axis.

To extend the analysis to the entire x-y plane, consider an arbitrary point $x = \langle x^*, y^* \rangle$. Also, define a *Whisker Line* as the line that runs through $F(y)$ in the direction of $u(y)$, for some value of y . If a whisker line runs through point x , this point is assigned the same protraction angle as would be calculated with $u(y)$ of that line.

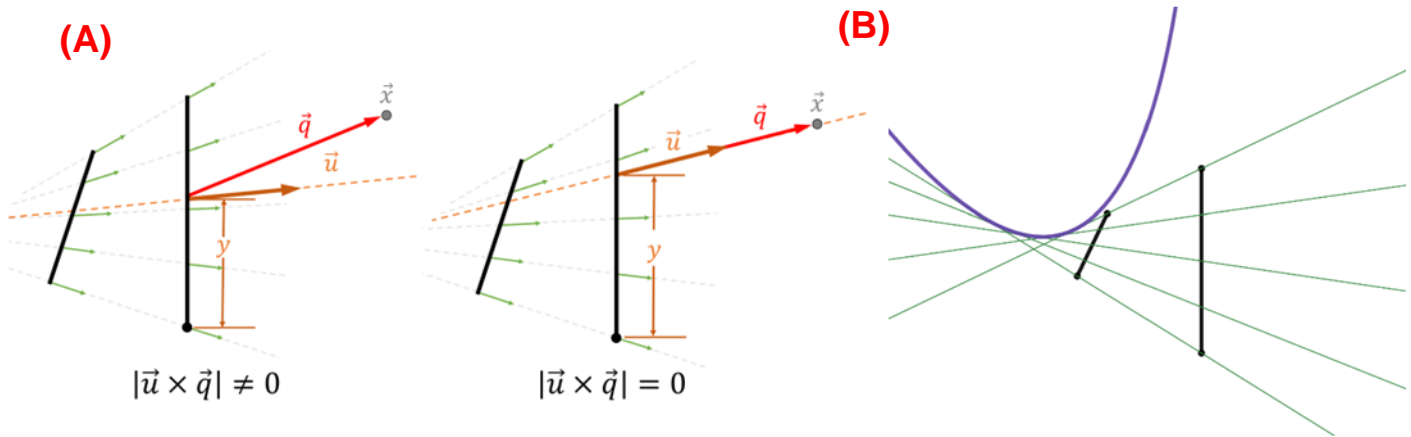


Figure 3.1: (A) The arbitrary point x is on a whisker line when $u(y)$ and $q(y)$ are parallel (B) Five whisker lines (green) and the boundary curve (purple). Note that the curve is tangent to all whiskers and frames.

To determine if x lies on a whisker line, we must construct a second vector $q(y)$ that runs from the face frame point $F(y)$ to x . x lies on a whisker line when $q(y)$ and $u(y)$ are collinear (Figure 3.3).

$$q(y) = x - F(y) = \langle x^*, y^* - y \rangle$$

When $q(y)$ and $u(y)$ are parallel, $|u(y) \times q(y)| = 0 \dots$

$$|u(y) \times q(y)| = -w_1 y^2 + (w_1 y^* - w_2 x^* + r_1)y + (-r_1 y^* + r_2 x^*) = 0$$

The above expression is quadratic with respect to y . Solving for y will show the location(s) on the face frame from which a whisker line extends to pass through \vec{x} .

$$y = \frac{w_1 y^* - w_2 x^* + r_1}{2w_1} \pm \frac{\sqrt{w_2^2 x^{*2} + (-2w_1 w_2)x^* y^* + w_1^2 y^{*2} + (-2r_1 w_2 + 4r_2 w_1)x^* + (-2r_1 w_1)y^* + r_1^2}}{-2w_1}$$

This equation gives insight to the geometry of the whisker frames by determining the *existence* of whiskers at any arbitrary point x . The *discriminant* (square root term) determines whether there can be one, two, or zero possible whisker lines passing through a given point. To visualize these possibilities as distinct regions of the x - y plane, the discriminant is set equal to zero and plotted. In other words, plotting all x^* and y^* where there is only one possible whisker line, to separate the regions where there are two and where there are none. Isolating the discriminant and setting it to zero yields the equation for a conic section.

$$w_2^2 x^{*2} + (-2w_1 w_2)x^* y^* + w_1^2 y^{*2} + (-2r_1 w_2 + 4r_2 w_1)x^* + (-2r_1 w_1)y^* + r_1^2 = 0$$

When plotted, it is revealed that the curve (Figure 3.1-C, purple) is tangent to all possible whisker lines. The region inside the curve is the region where no possible whiskers can cross

(imaginary solutions for y). This conic curve can be further classified by representing its equation in matrix form...

$$\vec{x}^T A \vec{x} = 0, \text{ where } \vec{x} = \begin{bmatrix} x \\ y \\ 1 \end{bmatrix} \text{ and } A = \begin{bmatrix} w_2^2 & -w_1 w_2 & -r_1 w_2 + 2r_2 w_1 \\ -w_1 w_2 & w_1^2 & -r_1 w_1 \\ -r_1 w_2 + 2r_2 w_1 & -r_1 w_1 & r_1^2 \end{bmatrix}$$

Two determinants must be calculated to fully classify a conic section in matrix form. The first

test is of the sub-matrix $A_{33} = \begin{bmatrix} w_2^2 & -w_1 w_2 \\ -w_1 w_2 & w_1^2 \end{bmatrix}$. If $\det A_{33} < 0$, the conic is a hyperbola. If

$\det A_{33} = 0$, it is a parabola. If $\det A_{33} > 0$, it is an ellipse. In this case $\det A_{33} = 0$, so the conic curve takes the form of a parabola for all non-degenerate cases.

The second test is for whether the conic is in a *degenerate* form. If $\det A = 0$, the conic is degenerate. To test A for degeneracy, we calculate the determinant of A...

$$\det A = -4w_1^2(r_1 w_2 - r_2 w_1)^2$$

We found that there exist certain input configurations that would result in the above expression being equal to zero, resulting in degeneracy. These configurations are discussed in the next section.

3.2 Degenerate configurations of the parabola cause all whiskers to converge to a point or be parallel

Recall a conic takes a *degenerate* form when its full matrix determinant is equal to zero, resulting in a curve that is neither parabolic nor like any other conic. In this model

$$\det A = -4w_1^2(r_1w_2 - r_2w_1)^2; \text{ when degenerate, } \det A = 0$$

There are multiple cases when this is true, each with its own geometric explanation. The trivial solution to $\det A = 0$ occurs when $w_1 = 0$. Expanded, $w_1 = (s \sin \theta)$, meaning that either $s = 0$ or $\theta = 0$ cause degeneracy in the boundary curve. These cases, visualized in Figure 3.2-(A,B), both collapse the boundary curve into a point where all whisker lines intersect. Note that $(\theta = 0)$ is fully feasible and occurs whenever the frames are parallel.

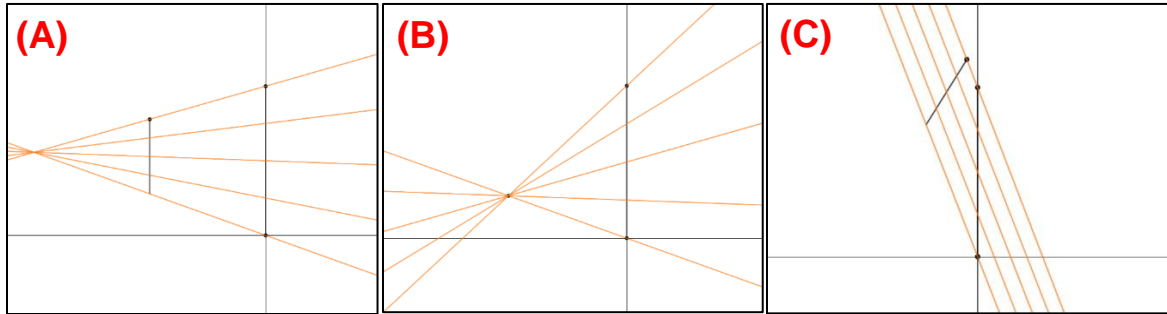


Figure 3.2: (A,B) Trivial degenerate forms of the boundary curve. (a) $\theta = 0$ and (b) $s = 0$ **(C)** Nontrivial degeneracy when $\mathbf{r} \in \text{span}(\mathbf{w})$

The curve is also degenerate in the case where $\pm(r_1w_2 - r_2w_1) = 0$. Assuming $w_1 \neq 0$, thus also $w_2 \neq 1$, degeneracy is a function of when r_1 and r_2 cause the term to equal zero. The term $(r_1w_2 - r_2w_1)$ is equal to $\det \begin{bmatrix} r_1 & w_1 \\ r_2 & w_2 \end{bmatrix}$, which is also equal to $\|\mathbf{r} \times \mathbf{w}\|$. For this term to equal zero, it would require \mathbf{r} and \mathbf{w} to be collinear. In other words, the curve is degenerate when $\mathbf{r} \in \text{span}(\mathbf{w})$ [Figure xx+3].

3.3 Non-degenerate cases of the whisker-tangent parabola permit visualization all possible whisker outputs

The existence of a tangent parabola (section 3.1), is an invariant property of all non-degenerate configurations of the whisker mechanism. This property, combined with the properties of all parabolas, offers a global understanding of all possible protractions generated by the system.

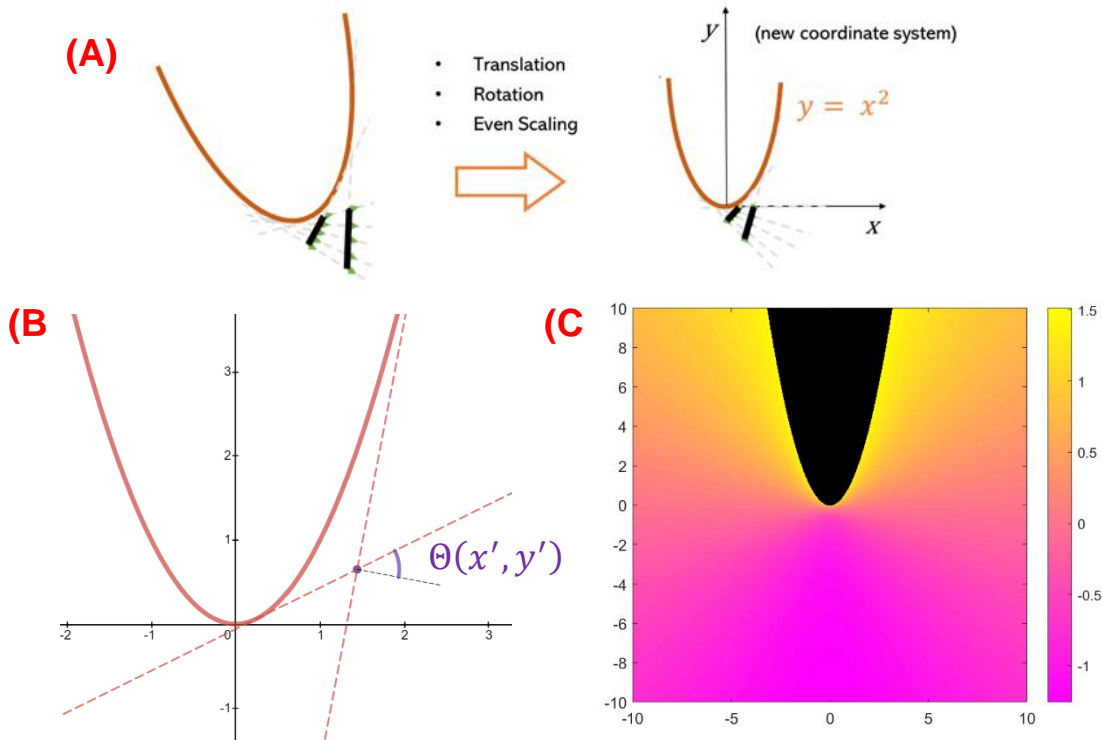


Figure 8: (A) Transformation strategy to convert an arbitrary boundary curve into the unit parabola $y=x^2$ (B) Geometric construction of protraction values relative to the parabola (C) Protraction generalized to the region outside the unit parabola. Color indicates protraction value between $-\pi/2$ and $\pi/2$.

Knowing that the non-degenerate boundary curve is always a parabola and given the geometric fact that all parabolas are *similar* (in other words, that any parabola can be superimposed by a uniform scaling and translation of the unit parabola $y = x^2$), analysis of whisker geometry can be reframed from the perspective of the unit parabola. Thus, aspects of *all* parabolas can be used to analyze the whisker geometry by linearly transforming the xy -plane such that the boundary curve becomes the unit parabola, which is the simplest parabola to analyze. It would

also glean generalized information about the nature of the whisker geometry. See the supplemental section S.3 for details on this transformation.

A new coordinate frame $\{x'y'\}$ is attached to the unit parabola such that the origin of $\{x'y'\}$ is on the parabolic vertex and the parabola is defined by $y' = x'^2$. Points *outside* the parabola are defined as the set of ordered pairs $\{(x', y') \in \mathbb{R} \mid y'^2 < x'\}$, and points *inside* the parabola are defined as the set of ordered pairs $\{(x', y') \in \mathbb{R} \mid y'^2 \geq x'\}$. Protraction, as first defined in section 3.2, can now be expressed as a function of x^{\wedge} and y^{\wedge} for all points outside the parabola, and yields the protraction angle at point (x', y') where an equivalent point $\Theta(y)$ on the face frame has been transformed onto. Protraction is defined below. See supplemental information for a derivation.

$$\Theta(y) = \Theta(x', y') = \arctan\left(2x' - 2\sqrt{x'^2 - y'}\right) - \arctan\left(2x' + 2\sqrt{x'^2 - y'}\right) + \frac{\pi}{2}$$

$\Theta(x', y')$ is a single, generalized function for protraction which outputs *all possible* angles producible by the Whisker Frames mechanism for all input parameters (r_1, r_2, s, θ) . Plotting this function in the normalized space $\{x'y'\}$ visualizes the range of outputs as a colormap, shown in Figure 3.3-C.

The normalized space presented above is offered for further analysis of the possible configuration trajectories for this mechanism but will not be elaborated upon further in this work.

3.4 The modified vector model positions the control frame in an elliptical pattern

As a further exploration of the geometric properties of this system, the following section will explore the constrained movement of the control frame in the modified vector model introduced in section 2.3.

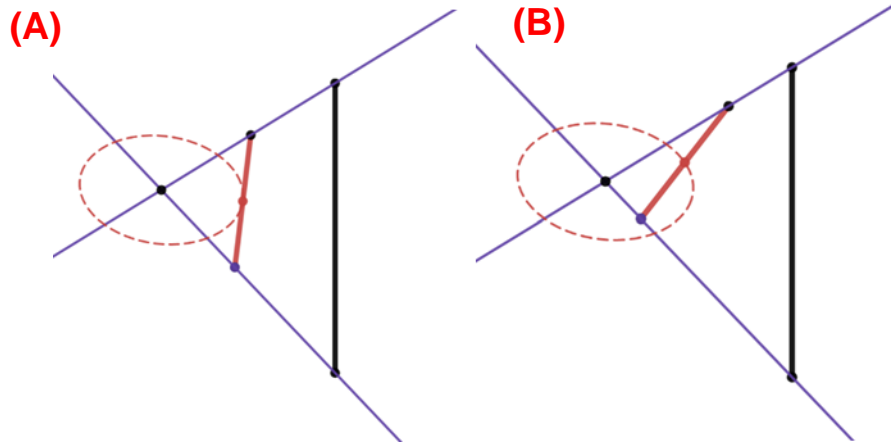


Figure 3.4: Multiple configurations of the constrained control frame reveal an elliptical path. The above plots show the constrained vector model for two values of θ . **(A)** a slightly negative value of θ . **(B)** a higher-magnitude negative value of θ . The ellipse (red, dashed) runs through the midpoint of every possible control frame.

Recall, when top and bottom angles are visualized, the dimensionality of the system is reduced to one degree of freedom, θ . To visualize the remaining degree of freedom, the following section will focus on the midpoint of the control frame. This will provide intuition for how the control frame moves through space when bound by top and bottom whisker.

Define a vector \mathbf{p} as the midpoint of the control frame, a distance $\frac{s}{2}$ away from \mathbf{r} . This is expressed mathematically by the following expression

$$\mathbf{p} = \mathbf{r} + \frac{s}{2} \hat{\mathbf{c}}, \text{ where } \hat{\mathbf{c}} = [-\sin \theta, \cos \theta]^T$$

Substituting in $\mathbf{r} = M\mathbf{w}...$

$$\mathbf{p} = \left[w_1 \left(\frac{\tan \alpha}{\tan \alpha - \tan \beta} \right) + w_2 \left(\frac{1}{\tan \beta - \tan \alpha} \right), w_1 \left(\frac{1}{\cot \beta - \cot \alpha} \right) + w_2 \left(\frac{\tan \beta}{\tan \beta - \tan \alpha} \right) \right]^T + \frac{s}{2} [-\sin \theta, \cos \theta]^T$$

To combine terms, \mathbf{w} is unpacked and θ terms are grouped.

$$\mathbf{p} = \left[\left(\frac{s \tan \alpha + \tan \beta}{2 \tan \alpha - \tan \beta} \right) \sin \theta + \left(\frac{s}{\tan \alpha - \tan \beta} \right) \cos \theta + \left(\frac{-1}{\tan \alpha - \tan \beta} \right), \left(\frac{s}{\cot \beta - \cot \alpha} \right) \sin \theta + \left(\frac{s \tan \alpha + \tan \beta}{2 \tan \alpha - \tan \beta} \right) \cos \theta + \left(\frac{-\tan \beta}{\tan \alpha - \tan \beta} \right) \right]^T$$

Regrouped as a matrix-vector expression...

$$\mathbf{p}(\theta) = \begin{bmatrix} \frac{s \tan \alpha + \tan \beta}{2 \tan \alpha - \tan \beta} & \frac{s}{\tan \alpha - \tan \beta} \\ \frac{s}{\cot \beta - \cot \alpha} & \frac{s \tan \alpha + \tan \beta}{2 \tan \alpha - \tan \beta} \end{bmatrix} \begin{bmatrix} \cos \theta \\ \sin \theta \end{bmatrix} + \begin{bmatrix} \frac{-1}{\tan \alpha - \tan \beta} \\ \frac{-\tan \beta}{\tan \alpha - \tan \beta} \end{bmatrix}$$

The above is the expression for an *ellipse* centered at the point $\left[\frac{-1}{\tan \alpha - \tan \beta}, \frac{-\tan \beta}{\tan \alpha - \tan \beta} \right]^T$ which is the intersection point of the top and bottom whisker lines. The major and minor axes are aligned to the spaces between these lines, as shown in the figure.

When the mechanism is constrained in this way, forcing two points along a segment to follow respective lines, the mechanism becomes equivalent to a classical mechanism known as “The Trammel of Archimedes”, which moves points in an elliptical trajectory and is the basis of simple mechanical ellipsographs.

3.5 Optimal trajectories for the control frame are found using both 3-DOF and 1-DOF models

Simulated trajectories were generated for a variety of values of smoothing constraints and the length ratio s . Trajectories were found for configurations over two search spaces: the 3-DOF model introduced in 2.2 with configuration vector $x = [r_1, r_2, \theta]$, and the 1-DOF (top and bottom whiskers matched exactly) model introduced in 2.3 with configuration vector $x_m = [\alpha, \beta, \theta]$.

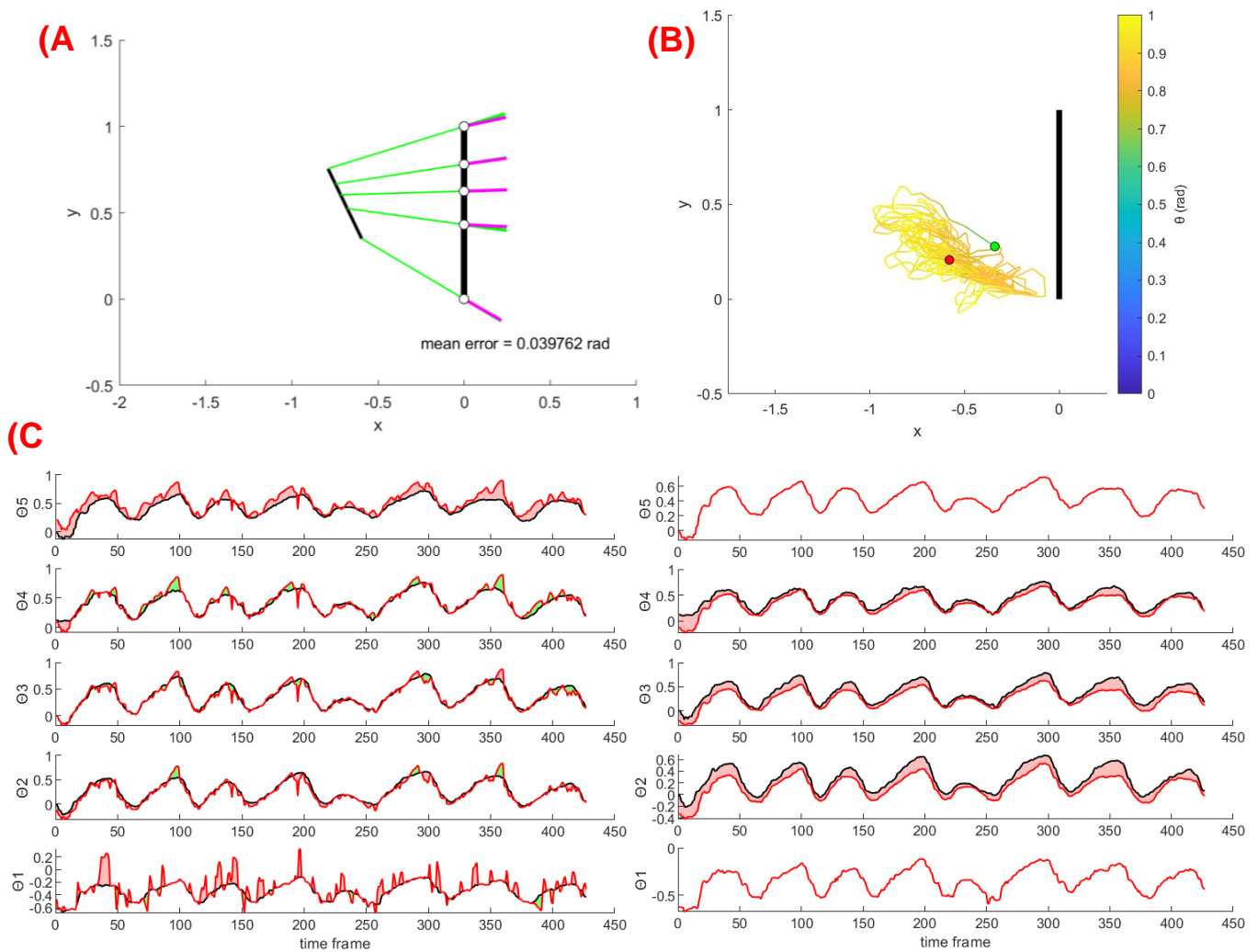


Figure 3.5: (A) A screenshot of an optimized trajectory using the 3-DOF method. At this frame, the mean error over the five whiskers is equal to 0.039 radians. (B) A plot of the trajectory for a 3-DOF trial with smoothing constraints enabled. The location of the line path indicates values of r_1 and r_2 , and the color indicates the value of the control frame rotation θ . (C) Protraction values for 1 through 5 (1 at the bottom, 5 at the top) over half the video length (frames 1 to 427 out of 855) for unconstrained, $s = 0.6$

trials of the 3-DOF model (left) and the 1-DOF model (right). Black curves mark the protraction of the biological whiskers from video, and the red curves mark the protraction of the mechanism at that point. Red and green fills mark parts of the curve where the mechanism and biological protractions are higher than the other, respectively. Note that regions without a fill are regions where the curves are equivalent.

The two models performed effectively, consistently finding configurations at each of the 855 frames that minimized the average error (as defined in 2.5) to less than 5 degrees. One such configuration, with a mean error of 0.039 radians (2 degrees) is shown in Figure 3.5-A. The arrangement of points and protractions of the single video clip analyzed in this work influenced the findings, as shown in Figure 3.5-B where optimal θ values of the control frame were often positive-valued. For each model, 100 trials were conducted over all permutations of the following constraint and s values.

Table 3.5-A: Trial constraint and s values

Parameter	Values
s	0.30, 0.45, 0.60, 0.75
R	0.05, 0.10, 0.20, 0.40, 0.80
dθ	$\pi/20$, $\pi/10$, $\pi/6$, $\pi/8$, $\pi/4$

Additionally, 5 more “unconstrained” trials were conducted varying the values of s shown in table 3.5-A (including an additional value of $s = 0.90$), but with large-valued constraints $R = 10$ and $d\theta = \frac{\pi}{2}$ to obviate the also effects of the smoothing constraints outlined in section 2.5. The results of these four sets of trials are expressed in Table 3.5-B by the lowest average error trials in each set, along with the constraints and s values for those trials.

Table 3.5-B: Minimum mean absolute error values with associated constraint and s values

Mode	Min. error [rad]	Min. error [deg]	s	R	dθ
1-DOF, constrained	0.0322	1.8449	0.75	0.05	$\pi/2$
3-DOF, constrained	0.0302	1.7303	0.75	0.05	$\pi/6$
1-DOF, unconstrained	0.0178	1.0199	0.90	10	$\pi/2$
3-DOF, unconstrained	0.0548	3.1398	0.75	10	$\pi/2$

In both constrained trial sets, error values minimized to a very similar value (around 1.8 degrees), both with $s = 0.75$ and $R = 0.05$. Interestingly, the tightest constraint of R was favored over other permutations, which might imply a positive effect to smoothing the trajectory. More clearly, s was found to decrease error as it increased to 0.75. Unconstrained trials did not behave as similarly, as shown above, with 1-DOF unconstrained producing the absolute lowest average of 1.019 degrees, and the 3-DOF producing a minimum approximately three times larger. Despite this discrepancy, all four trial sets produce an acceptable result that successfully replicates the majority of biological orientations tested in this study.

Though the two models performed roughly similarly, they generated very different trajectories. This is illustrated in Figure 3.5-C, where biological and mechanism protraction values for all whiskers in an unconstrained trial are plotted. The 3-DOF model is shown on the left and 1-DOF model is shown on the right. Notably, the “sign” of the error (error is quantified by absolute value, but the sign of the deviation is visualized by fill color in the figure) in the 3-DOF trial oscillates between positive and negative, and lightly increases in magnitude from the bottom to top whisker. Contrarily, the 1-DOF trial has exactly zero error in its top and bottom whiskers, which is by design. For the video data studied in this work, it is observed that the middle whiskers consistently lag under the biological protractions. This is because the protractions are

limited to a maximum value interpolated between α and β , preventing the mechanism from producing protractions greater than that maximum.

4. Discussion

4.1 Hardware model and extended applications

As evidenced by the stated equivalence between the hardware model defined in 2.1 and the vector models defined in 2.2 and 2.3, the core function of the whisker frames mechanism is to constrain lines between pairs of planar points. The “rotating joint” and “control joint” do not necessarily need to lie on the control and face frames respectively, so long as there are no additional constraints placed on the line defined in-between the joint pair.

One scope-defining assumption made for this work is that the frames should be straight lines. This assumption was made for simplicity, and is the root cause of many of the neat algebraic and geometric properties of the system, e.g. the parabola tangent to all whiskers. However, there is no physical constraint on what shape the frames must be, as all lines will still be oriented through pairs of corresponding points regardless of their location in space. Having straight-line frames also imposes a difficulty, as it requires projecting reference biological basepoints onto an axis they may be far away from, incorporating some error into values that are subsequently taken as ground-truth. One solution currently in development is to model the control frame and face frame as *circles* instead of straight lines. This is beneficial for three reasons: (1) modeling as a circle adds an additional constant parameter of *curvature* which could be varied to best-project the basepoints onto a circle arc, reducing projection error. (2) A curvature near or at zero results in straight-line frames, which would contribute all behaviors discussed in this work as a subset of the circular behaviors. (3) Though transitioning away from straight-line frames would erase the parabolic tangent, we have found that the circular geometry gives rise to a *non-parabolic conic section* (hyperbola or ellipse) tangent to all whiskers, which could work to create a generalized space similar to that proposed for this work in section 3.1.

Another possible venture elevates this planar mechanism to three dimensions by replacing rotating joints with spherical joints and rotating-sliding joints with spherical-sliding joints. Here, instead of whiskers being constrained along corresponding locations on two lines, whiskers would be constrained between corresponding locations on two planes, which would allow for different row behaviors. This solution is currently infeasible due to the lack of kinematic multi-row data and the difficulties of controlling a 6-dof “control plane”, but is an interesting problem to model for the time being.

4.2 Geometric insights

The “normalized space” $\{x'y'\}$ presented in section 3.3 is useful for visualizing the output space of the mechanism, where all possible frames lie on the pencil of tangents to the parabola, and all possible protractions are visualized as the color values those tangents move through. In a previous iteration of biological comparisons, this map was used as the search space for finding optimal configurations of the mechanism, but this was abandoned for the more straightforward search outlined in section 2.5. The normalized space is still offered in this work as an object for further analysis and could be an important tool in mapping neural pathways, as discussed in 4.4.

4.3 Trajectory optimization

With low values of mean error averaged over the trial sets, the mechanism performed effectively. The qualification for that statement is informed by (1) a low minimum average error with respect to the magnitude of the observed whisker span and (2) the timescale on which the reference motions are tracked. The biological data studied in this paper, a single 855-frame video captured in high-speed at 600 fps, spans a total recording time of approximately 1.42 seconds. The mouse whisks approximately 16 times in this short window, suggesting that

tracking error would be a limitation that might eclipse the low positional errors of this mechanism in a real-time hardware implementation.

The smoothing constraints played an unexpected role in low-error results, as several of the lowest-error trials retained tight constraints and the next unconstrained 3-DOF trial did not minimize error as expected. One explanation for this may be that maximally error-optimizing trajectories are non-unique, and the jagged trajectories generated in unconstrained trials might generate more outlier errors than constrained trials. This may also be an error in the nonlinear optimizer used for 3-DOF trials. In any case, constraints were successful in reducing bifurcations and “smoothing” the generated trajectory to a physically realizable trajectory.

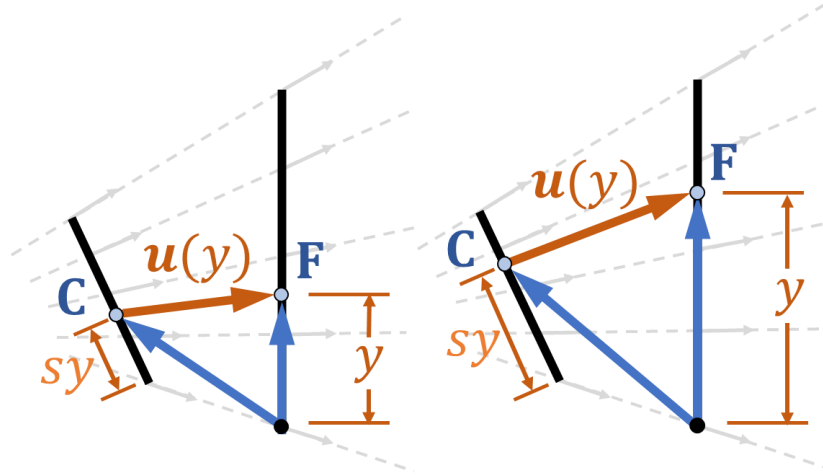
4.4 Biological analogy and dimensionality reduction

The analysis presented in this work is a study of a biomimetic kinematics mechanism that is proven to *mimic* the motions of real-life rodent vibrissa. It is not a statement of equivalence between the mechanics of the rodent mystacial pad and that of the mechanism, though the design of the mechanism was inspired by the vibrissal follicle musculature. However, an important consideration of this work is whether insights on biology could be *inferred* by analogizing the control and output of this model to motor control pathways in rodents. Of particular interest is the concept of *muscular synergies* in this analogy. Muscular synergies refer to the coordinated activations of many muscles as part of a single control pathway, effectively reducing the dimensionality of said muscle group by affecting a single motion. Modeling such a pathway is well outside the scope of this work, but the intended motions (protraction, spread) generated as a function of $[r_1, r_2, \theta]$ configuration could serve as a “task space” onto which neurological data could be mapped for some observed whisking motion. This work offers three spaces with which the 72-dof rat mystacial pad can be reduced to three degrees of freedom: the 3-DOF space, $\mathbf{x} = [r_1, r_2, \theta]$, the modified space $\mathbf{x}_m = [\alpha, \beta, \theta]$, and the normalized $\{x'y'\}$ space

discussed in section 3.3, into which two-dimensional information can be mapped. An associated mapping to protraction and spread can be modeled by the relations established in 2.2.

5. Supplemental Information and Derivations

S.1: Derivation of $\mathbf{u}(y)$ and \mathbf{w} vectors



Because the ratio of the length of the control frame and face frame is fixed (the ratio is s), all distances on the control frame are scaled by s , with respect to their corresponding points on the face frame. Specifically, a point on the face frame a distance y from the origin corresponds to a point on the control frame a distance (sy) from the bottom of the control frame. Thus, each point on the control frame has a unique corresponding point on the face frame; these corresponding pairs of points are denoted $\mathbf{C}(y)$ and $\mathbf{F}(y)$, respectively:

$$\mathbf{F}(y) = y\hat{\mathbf{j}} \quad \text{where } \hat{\mathbf{j}} = \langle 0, 1 \rangle$$

$$\mathbf{C}(y) = \mathbf{r} + (sy)\hat{\mathbf{c}}, \quad \text{where } \hat{\mathbf{c}} = \langle -\sin\theta, \cos\theta \rangle$$

An expression for protraction was derived by constructing a vector $\mathbf{u}(y)$ by subtracting a corresponding control frame point from a point on the face frame (y -position).

$$\mathbf{u}(y) = \mathbf{F}(y) - \mathbf{C}(y)$$

$$\mathbf{u}(y) = y\hat{\mathbf{j}} - (\mathbf{r} + (sy)\hat{\mathbf{c}})$$

$$\mathbf{u}(y) = (\hat{\mathbf{j}} - s\hat{\mathbf{c}})y - \mathbf{r}$$

$$\mathbf{u}(y) = \mathbf{w}y - \mathbf{r} \quad \text{where } \mathbf{w} = (\hat{\mathbf{j}} - s\hat{\mathbf{c}})$$

In component form, $\mathbf{u}(y) = \langle w_1y - r_1, w_2y - r_2 \rangle = \langle (s \sin \theta)y - r_1, (1 - \cos \theta)y - r_2 \rangle$

S.2: Derivation of the vector \mathbf{r} for the modified vector model

To find \mathbf{r} , a starting assumption is made that \mathbf{r} lies on the line spanned by the bottom whisker.

In other words,

$$\mathbf{r} = a \begin{bmatrix} \cos \beta \\ \sin \beta \end{bmatrix}, \text{ where } a \text{ is some scalar distance}$$

This distance is found by trigonometry, producing the following equation:

$$\mathbf{r} = \left(\frac{s \cos(\alpha - \theta) - \cos \alpha}{\sin(\alpha - \beta)} \right) \begin{bmatrix} \cos \beta \\ \sin \beta \end{bmatrix}$$

Expanded, we can reuse the vector $\mathbf{w} = \langle s \sin \theta, 1 - s \cos \theta \rangle$ in our expression

$$\mathbf{r} = \left(\frac{\cos \alpha (1 - s \cos \theta) + \sin \alpha (s \sin \theta)}{\sin(\alpha - \beta)} \right) \begin{bmatrix} \cos \beta \\ \sin \beta \end{bmatrix}$$

$$\mathbf{r} = \left(\frac{w_1 \sin \alpha + w_2 \cos \alpha}{\sin(\alpha - \beta)} \right) \begin{bmatrix} \cos \beta \\ \sin \beta \end{bmatrix}$$

Multiplying into the vector after expanding the $\sin(\alpha - \beta)$ term, the following expression is reached

$$\mathbf{r} = \left[w_1 \left(\frac{\tan \alpha}{\tan \alpha - \tan \beta} \right) + w_2 \left(\frac{1}{\tan \beta - \tan \alpha} \right), w_1 \left(\frac{1}{\cot \beta - \cot \alpha} \right) + w_2 \left(\frac{\tan \beta}{\tan \beta - \tan \alpha} \right) \right]^T$$

Rearranged into a matrix-vector product, \mathbf{w} is isolated...

$$\mathbf{r} = \begin{bmatrix} \frac{\tan \alpha}{\tan \alpha - \tan \beta} & \frac{1}{\tan \beta - \tan \alpha} \\ \frac{1}{\cot \beta - \cot \alpha} & \frac{\tan \beta}{\tan \beta - \tan \alpha} \end{bmatrix} \mathbf{w} = M \mathbf{w}$$

Note that terms $\tan \alpha$ and $\tan \beta$ correspond to the *slopes* of the lines drawn by angles α and β .

$\mathbf{u}(y)$ can now be found by the following relation

$$\mathbf{u}(y) = \mathbf{w}y - \mathbf{r} = \mathbf{w}y - M\mathbf{w} = (yI)\mathbf{w} - M\mathbf{w}$$

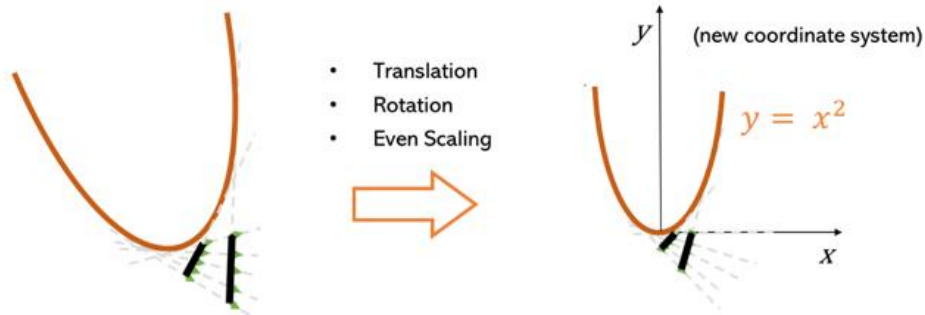
$$\mathbf{u}(y) = (yI - M)\mathbf{w}$$

Keeping s fixed, \mathbf{w} is only a function of θ . As a result, $\mathbf{u}(y)$ is only shaped by one degree of freedom, θ .

Like before, protraction is found by

$$\theta(y) = \tan^{-1} \frac{u_2}{u_1}$$

S.3: Homogenous Transformation of conic curves to the unit parabola $y=x^2$



Performing this transformation requires three pieces of information from the parabola. They are the position of the parabolic vertex, the angle of the parabolic axis, and the scale factor (1-dimensional factor by which the boundary curve parabola is larger than the unit parabola).

These three pieces of information will form a transformation composed of a translation, a rotation, and a uniform scaling of the x-y plane, applying not only to the curve but also to the face frame, control frame, and the infinite set of possible whiskers.

Analytic equations for the vertex, axis angle, and scale factor are as follows...

$$\mathbf{V} = \left\langle \frac{w_2^2(r_1 w_2 + r_2 w_1)}{(w_1^2 + w_2^2)}, \frac{r_1 w_1^3 - 2r_2 w_1^2 w_2 - r_2 w_2^3}{(w_1^2 + w_2^2)} \right\rangle$$

$$\alpha = \tan^{-1} \left(\frac{-w_1}{w_2} \right)$$

$$F = \|\mathbf{r}\| \sin(\zeta - \alpha) \left(\frac{4w_1}{w_1^2 + w_2^2} \right), \quad \text{where } \zeta = \tan^{-1} \left(\frac{-r_2}{r_1} \right)$$

The transformation resulting in the unit parabola would thus consist of a translation by $-\mathbf{V}$, a rotation by $-\alpha$, and a uniform scaling by the scale factor $1/F$.

To transform a homogenous coordinate vector $x = \begin{bmatrix} x \\ y \\ 1 \end{bmatrix}$ from xy to $\{x'y'\}$ coordinates, the

following transformation is applied...

$$x' = Tx$$

$$\text{where } T = \begin{bmatrix} 1/F & 0 & 0 \\ 0 & 1/F & 0 \\ 0 & 0 & 1 \end{bmatrix} \begin{bmatrix} \cos(-\alpha) & -\sin(-\alpha) & 0 \\ \sin(-\alpha) & \cos(-\alpha) & 0 \\ 0 & 0 & 1 \end{bmatrix} \begin{bmatrix} 1 & 0 & -V_1 \\ 0 & 1 & -V_2 \\ 0 & 0 & 1 \end{bmatrix}$$

See the next section for derivations of each of the three transformation parameters.

S.4: Derivations of transformation parameters for $\{xy\} \rightarrow \{x'y'\}$

Axis Angle Derivation

α is the angle of the axis of the parabola with respect to the y axis. When rotated by $-\alpha$, the axis of the parabola in $\{xy\}$ becomes vertical, like that of the unit parabola $y' = x'^2$. The direction of the parabola's axis can be derived from its conic equation via the principal axis theorem for conics.

Recall, the matrix form of the parabolic curve:

$$\vec{x}^T A \vec{x} = 0, \text{ where } \vec{x} = \begin{bmatrix} x \\ y \\ 1 \end{bmatrix} \text{ and } A = \begin{bmatrix} w_2^2 & -w_1 w_2 & -r_1 w_2 + 2r_2 w_1 \\ -w_1 w_2 & w_1^2 & -r_1 w_1 \\ -r_1 w_2 + 2r_2 w_1 & -r_1 w_1 & r_1^2 \end{bmatrix}$$

By the principal axis theorem, the principal axes of this conic are spanned by the eigenvectors

of the 2x2 submatrix $A_{33} = \begin{bmatrix} w_2^2 & -w_1 w_2 \\ -w_1 w_2 & w_1^2 \end{bmatrix}$. The eigenvalues and associated eigenvectors

are below:

$$\text{for } \lambda_1 = (w_1^2 + w_2^2), \quad \mathbf{v} = \begin{bmatrix} 1 \\ \frac{w_2}{w_1} \end{bmatrix}$$

$$\text{for } \lambda_2 = 0, \quad \mathbf{v} = \begin{bmatrix} 1 \\ -\frac{w_1}{w_2} \end{bmatrix}$$

These two vectors correspond to lines of slope $\frac{w_2}{w_1}$ and $\frac{-w_1}{w_2}$, respectively. These slopes are

inverse to each other; thus, they are perpendicular. The line of slope $\frac{w_2}{w_1}$, otherwise known as

$\text{span}(\mathbf{w})$, is shown to be parallel to the parabolic axis. The angle α is thus the angle between \mathbf{w} and the vertical axis, defined:

$$\alpha = \tan^{-1}\left(\frac{-w_1}{w_2}\right)$$

Vertex Expression

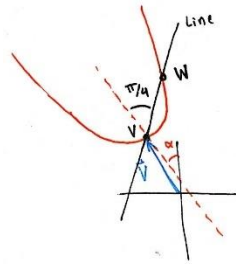
The parabolic vertex is located at the vector V , expressed below.

$$V = \left[\frac{w_2^2(r_1 w_1 + r_2 w_2)}{w_1^2 + w_2^2}, \frac{r_1 w_1^3 - 2r_2 w_1^2 w_2 - r_2 w_2^3}{w_1^2 + w_2^2} \right]^T$$

Scale Factor Derivation

The 1D scale factor F is the factor by which distances in $\{x',y'\}$ are scaled to equal corresponding distances in $\{xy\}$. This factor is used to scale down (by $1/F$) the parabola of arbitrary size in $\{xy\}$ to the unit parabola $y' = x'^2$.

Given expressions for components of V and the axis angle α , the following geometry is constructed...



A line L is drawn through V and oriented $\pi/4$ from the parabolic axis. This line intersects the parabola at V and at a second point W . On the unit parabola $y' = x'^2$, W would lie on the point $(1,1)$, a distance $\sqrt{2}$ from V . In $\{xy\}$, this distance would be scaled by F .

Therefore, F is calculated as: $F = \frac{\overline{VW}}{\sqrt{2}}$

Using a symbolic math package, this distance was found to simplify to the following expression...

$$F = \sqrt{\frac{16w_1^2(r_1w_2 - r_2w_1)^2}{(w_1^2 + w_2^2)^3}}$$

This expression can be unpacked to provide a clearer geometric statement...

$$F = (r_1w_2 - r_2w_1) \sqrt{\frac{1}{w_1^2 + w_2^2}} \sqrt{\frac{16w_1^2}{(w_1^2 + w_2^2)^2}}$$

$$\begin{aligned}
&= \frac{\|\mathbf{r} \times \mathbf{w}\|}{\sqrt{w_1^2 + w_2^2}} \left(\frac{4w_1}{w_1^2 + w_2^2} \right) \\
&= \frac{\|\mathbf{r}\| * \|\mathbf{w}\| * \sin(\zeta - \alpha)}{\|\mathbf{w}\|} \left(\frac{4w_1}{w_1^2 + w_2^2} \right)
\end{aligned}$$

...where ζ and α are the angles of \mathbf{r} and \mathbf{w} with respect to the y axis.

$$F = \|\mathbf{r}\| \sin(\zeta - \alpha) \left(\frac{4w_1}{w_1^2 + w_2^2} \right)$$

The resulting equation can be interpreted to mean that the scale factor F is proportional to the orthogonal distance between \mathbf{r} and the axis spanned by \mathbf{w} . This reaffirms the degenerate case when $\mathbf{r} \in \text{span}(\mathbf{w})$, as this orthogonal distance would equal zero, resulting in $F = 0$.

References

1. Vincent, S.B., *The tactile hair of the white rat*. Journal of Comparative Neurology, 1913. **23**(1): p. 1-35.
2. Welker, W.I., *Analysis of sniffing of the albino rat*. Behavioural Brain Research, 1964. **22**: p. 223-244.
3. Paxinos, G., *The Rat Nervous System, 2nd edition*. 1995, San Diego: Academic Press.
4. Prusky, G.T., et al., *Variation in visual acuity within pigmented, and between pigmented and albino rat strains*. Behavioural Brain Research, 2002. **136**(2): p. 339-348.
5. Prusky, G.T., P.W.R. West, and R.M. Douglas, *Behavioral assessment of visual acuity in mice and rats*. Vision Research, 2000. **40**(16): p. 2201-2209.
6. Vincent, S.B., *The tactile hair of the white rat*. J. Comp. Neur., 1913. **23**(1): p. 1-38.
7. Welker, W.I., *Analysis of sniffing of the albino rat*. Behaviour, 1964. **22**: p. 223-244.
8. Wineski, L., *Movements of the cranial vibrissae in the golden hamster (Mesocricetus auratus)*. . J Zool (Lond) 1983. **200**: p. 261–280.
9. Brecht, M., B. Preilowski, and M.M. Merzenich, *Functional architecture of the mystacial vibrissae*. Behav. Brain Res., 1997. **84**: p. 81-97.
10. Towal, R.B., et al., *The Morphology of the Rat Vibrissal Array: A Model for Quantifying Spatiotemporal Patterns of Whisker-Object Contact*. PLOS Computational Biology, 2011. **7**(4).
11. Berg, R.W. and D. Kleinfeld, *Rhythmic whisking by rat: Retraction as well as protraction of the vibrissae is under active muscular control*. Journal of Neurophysiology, 2003. **89**(1): p. 104-117.
12. Carvell, G.E. and D.J. Simons, *BIOMETRIC ANALYSES OF VIBRISSAL TACTILE DISCRIMINATION IN THE RAT*. Journal of Neuroscience, 1990. **10**(8): p. 2638-2648.
13. Ebara, S., et al., *Similarities and differences in the innervation of mystacial vibrissal follicle-sinus complexes in the rat and cat: A confocal microscopic study*. Journal of Comparative Neurology, 2002. **449**(2): p. 103-119.
14. Rice, F.L., et al., *Comprehensive immunofluorescence and lectin binding analysis of vibrissal follicle sinus complex innervation in the mystacial pad of the rat*. Journal of Comparative Neurology, 1997. **385**(2): p. 149-184.
15. Rice, F.L., A. Mance, and B.L. Munger, *A Comparative Light Microscopic Analysis of the Sensory Innervation of the Mystacial Pad .1. Innervation of Vibrissal Follicle-Sinus Complexes*. Journal of Comparative Neurology, 1986. **252**(2): p. 154-174.
16. Leiser, S.C. and K.A. Moxon, *Responses of trigeminal ganglion neurons during natural whisking behaviors in the awake rat*. Neuron, 2007. **53**(1): p. 117-133.
17. Lichtenstein, S.H., G.E. Carvell, and D.J. Simons, *RESPONSES OF RAT TRIGEMINAL GANGLION NEURONS TO MOVEMENTS OF VIBRISSAE IN DIFFERENT DIRECTIONS*. Somatosensory and Motor Research, 1990. **7**(1): p. 47-65.
18. Szwed, M., et al., *Responses of trigeminal ganglion neurons to the radial distance of contact during active vibrissal touch*. Journal of Neurophysiology, 2006. **95**(2): p. 791-802.
19. Bush, N.E., et al., *Decoupling kinematics and mechanics reveals coding properties of trigeminal ganglion neurons in the rat vibrissal system*. Elife, 2016. **5**.
20. Campagner, D., et al., *Prediction of primary somatosensory neuron activity during active tactile exploration*. Elife, 2016. **5**.
21. Severson, K.S., et al., *Active Touch and Self-Motion Encoding by Merkel Cell-Associated Afferents*. Neuron, 2017. **94**(3): p. 666-+.

22. Gutnisky, D.A., et al., *Mechanisms underlying a thalamocortical transformation during active tactile sensation*. Plos Computational Biology, 2017. **13**(6).
23. Sofroniew, N.J., et al., *Natural Whisker-Guided Behavior by Head-Fixed Mice in Tactile Virtual Reality*. Journal of Neuroscience, 2014. **34**(29): p. 9537-9550.
24. Sofroniew, N.J., et al., *Neural coding in barrel cortex during whisker-guided locomotion*. Elife, 2015. **4**.
25. Vaxenburg, R., et al., *Dynamic cues for whisker-based object localization: An analytical solution to vibration during active whisker touch*. Plos Computational Biology, 2018. **14**(3).
26. Maravall, M. and M.E. Diamond, *Algorithms of whisker-mediated touch perception*. Current Opinion in Neurobiology, 2014. **25**: p. 176-186.
27. LWJ, B., et al., *Anatomical pathways involved in generating and sensing rhythmic whisker movements* Front Integr Neurosci 2011. **5**(53).
28. Moore, J.D., et al., *Hierarchy of orofacial rhythms revealed through whisking and breathing*. Nature, 2013. **497**(7448): p. 205-+.
29. Grant, R.A., et al., *Active Touch Sensing in the Rat: Anticipatory and Regulatory Control of Whisker Movements During Surface Exploration*. Journal of Neurophysiology, 2009. **101**(2): p. 862-874.
30. Grant, R.A., B. Mitchinson, and T.J. Prescott, *The development of whisker control in rats in relation to locomotion*. Developmental Psychobiology, 2012. **54**(2): p. 151-168.
31. Grant, R.A., A.L. Sperber, and T.J. Prescott, *The role of orienting in vibrissal touch sensing*. Frontiers in Behavioral Neuroscience, 2012. **6**.
32. Mitchinson, B., et al., *Feedback control in active sensing: rat exploratory whisking is modulated by environmental contact*. Proceedings of the Royal Society B-Biological Sciences, 2007. **274**(1613): p. 1035-1041.
33. Mitchinson, B. and T.J. Prescott, *Whisker Movements Reveal Spatial Attention: A Unified Computational Model of Active Sensing Control in the Rat*. Plos Computational Biology, 2013. **9**(9).
34. Sachdev, R.N.S., et al., *Unilateral vibrissa contact: changes in amplitude but not timing of rhythmic whisking*. Somatosensory and Motor Research, 2003. **20**(2): p. 163-169.
35. Sachdev, R.N.S., T. Sato, and F.F. Ebner, *Divergent movement of adjacent whiskers*. Journal of Neurophysiology, 2002. **87**(3): p. 1440-1448.
36. Sellien, H., D.S. Eshenroder, and F.F. Ebner, *Comparison of bilateral whisker movement in freely exploring and head-fixed adult rats*. Somatosensory and Motor Research, 2005. **22**(3): p. 97-114.
37. Towal, R.B. and M.J. Hartmann, *Right-left asymmetries in the whisking behavior of rats anticipate head movements*. Journal of Neuroscience, 2006. **26**(34): p. 8838-8846.
38. Towal, R.B. and M.J.Z. Hartmann, *Variability in velocity profiles during free-air whisking behavior of unrestrained rats*. Journal of Neurophysiology, 2008. **100**(2): p. 740-752.
39. Deutsch, D., et al., *Fast Feedback in Active Sensing: Touch-Induced Changes to Whisker-Object Interaction*. Plos One, 2012. **7**(9).
40. Carvell, G.E. and D.J. Simons, *TASK-RELATED AND SUBJECT-RELATED DIFFERENCES IN SENSORIMOTOR BEHAVIOR DURING ACTIVE TOUCH*. Somatosensory and Motor Research, 1995. **12**(1): p. 1-9.
41. Carvell, G.E., et al., *ELECTROMYOGRAPHIC ACTIVITY OF MYSTACIAL PAD MUSCULATURE DURING WHISKING BEHAVIOR IN THE RAT*. Somatosensory and Motor Research, 1991. **8**(2): p. 159-164.
42. Dorfl, J., *THE MUSCULATURE OF THE MYSTACIAL VIBRISSAE OF THE WHITE-MOUSE*. Journal of Anatomy, 1982. **135**(AUG): p. 147-154.

43. Simony, E., et al., *Temporal and Spatial Characteristics of Vibrissa Responses to Motor Commands*. Journal of Neuroscience, 2010. **30**(26): p. 8935-8952.
44. Mitchinson, B., et al., *Perception of Simple Stimuli Using Sparse Data from a Tactile Whisker Array*. 2013.
45. N'Guyen, S., P. Pirim, and J.-A. Meyer, *Tactile Texture Discrimination in the Robot-rat Psikharpax*. 2010. 74-81.
46. Pearson, M.J., et al., *SCRATCHbot: Active tactile sensing in a whiskered mobile robot*. Proceedings SAB, 2010. **LNAI 6226**: p. 93-103.
47. Birdwell, J.A., et al., *Biomechanical Models for Radial Distance Determination by the Rat Vibrissal System*. Journal of Neurophysiology, 2007. **98**(4): p. 2439-2455.
48. Evans, M., et al., *The effect of whisker movement on radial distance estimation: a case study in comparative robotics*. Frontiers in Neurorobotics, 2013. **6**(12).
49. Huet, L.A., J.W. Rudnicki, and M.J.Z. Hartmann, *Tactile Sensing with Whiskers of Various Shapes: Determining the Three-Dimensional Location of Object Contact Based on Mechanical Signals at the Whisker Base*. Soft Robot, 2017. **4**(2): p. 88-102.
50. Yi, Y., *Texture Classification with Biomimetic Whisker Sensor*, in *Mechanical Engineering*. 2019, Northwestern University.
51. Hanke, W., et al., *Harbor seal vibrissa morphology suppresses vortex-induced vibrations*. J Exp Biol, 2010. **213**(Pt 15): p. 2665-72.